Materials Science & Engineering R 165 (2025) 101004

Contents lists available at ScienceDirect

Materials Science & Engineering R

journal homepage: www.elsevier.com/locate/mser

Highly elastic, lightweight, and high-performance all-aerogel triboelectric nanogenerator for self-powered intelligent fencing training

Muqi Chen [a,b,1], Minglan Ji [a,c,1], Lijun Huang [a,c], Ning Wu [a,c], Tao Jiang [a,c,d], Chengyu Li [a,c], Wanpeng Li [a,c], Boyang Yu [a,c], Jianjun Luo [a,c,d,*], Xiaoyi Li [b,**], Zhong Lin Wang [a,d,*]

[a] *Beijing Institute of Nanoenergy and Nanosystems, Chinese Academy of Sciences, Beijing 101400, PR China*
[b] *College of Materials Science and Engineering, Ocean University of China, Qingdao Key Laboratory of Marine Extreme Environment Materials, Qingdao 266100, PR China*
[c] *School of Nanoscience and Engineering, University of Chinese Academy of Sciences, Beijing 100049, PR China*
[d] *Guangzhou Institute of Blue Energy, Knowledge City, Huangpu District, Guangzhou 510555, PR China*

ARTICLE INFO

Keywords:
Triboelectric nanogenerator
Intelligent sports
Energy harvesting
Self-powered system
Aerogel
Wearable electronics

ABSTRACT

With the rapid advancement of the Internet of Things and big data, the sports industry is undergoing a digital transformation. Here, we report a highly elastic, lightweight, and high-performance all-aerogel triboelectric nanogenerator (AA-TENG) for self-powered sensing in intelligent fencing training. Utilizing simple yet effective freeze-drying strategies for fabricating cellulose/carbon nanotube and poly(vinylidene fluoride-co-trifluoroethylene) (PVDF-TrFE) aerogels, the resulting AA-TENG demonstrates an ultralow density of 7.92×10^{-3}g/cm^3, exceptional elasticity ($\geq$90 % height retention) and thermal insulation performance. Moreover, the electrical output performance is significantly enhanced by 57 %, attributed to the increased β-phase content (88.95 %) in the PVDF-TrFE aerogel. Furthermore, a self-powered wireless fencing strike analysis system using convolutional neural network algorithm is developed to accurately classify three types of fencing strikes, enabling more flexible and precise competition judgment and training analysis. This work provides new insights into the application of self-powered systems in intelligent sports and big data analysis, with the potential to significantly impact the global sports industry.

1. Introduction

The integration of the Internet of Things (IoTs) [1,2] and big data [3,4] has ushered sports into the era of digital information [5–11]. This transformation has driven innovations in exercise methodologies [12], sports concepts [13], and the widespread adoption of intelligent devices [14]. Sports digitization relies on sensor networks deployed across venues [15], equipment [16], and athletes [17] to collect real-time performance data. Through advanced data analysis, these technologies enable precise performance evaluation, personalized training regimens, and objective decision-making in competitions. However, conventional sensors are generally powered by batteries, which could cause high maintenance costs and environmental issues, and affect the wearable performance [18,19]. To overcome these challenges, there is an urgent need for lightweight, maintenance-free sensors that enhance efficiency and sustainability in sports systems.

In 2012, Prof. Zhong Lin Wang introduced the triboelectric nanogenerator (TENG)[20], which operates based on the coupling effect of triboelectrification and electrostatic induction, enabling the conversion of mechanical energy into electrical energy [21–23]. With numerous advantages such as high efficiency, diverse structures, and a broad selection of material options [24–30], TENGs can be utilized to harvest various kinds of mechanical energy during sports activities. By directly converting mechanical stimuli (such as human motions, object vibrations, and fluid flows) into electrical signals [31–33], TENGs can also function as self-powered sensors, which is crucial for the development of maintenance-free systems. Consequently, TENG technology presents a promising power solution for the emerging fields of IoTs, sensor

* Corresponding authors at: Beijing Institute of Nanoenergy and Nanosystems, Chinese Academy of Sciences, Beijing 101400, PR China.
** Corresponding author.
E-mail addresses: luojianjun@binn.cas.cn (J. Luo), lixiaoyi@ouc.edu.cn (X. Li), zhong.wang@mse.gatech.edu (Z.L. Wang).
[1] These authors contributed equally to this work.

https://doi.org/10.1016/j.mser.2025.101004
Received 13 March 2025; Received in revised form 13 April 2025; Accepted 21 April 2025
Available online 30 April 2025

networks, and intelligent sports, where large amounts of distributed devices are essential [34–36].

Among various TENG materials, aerogels have demonstrated significant potential for pressure-sensing applications [37–39]. Their unique three-dimensional porous structure can provide high sensing sensitivity, as the gradual increase in contact area during compression enhances TENG output [40]. However, most aerogels suffer from brittleness, low mechanical strength, and limited compressibility [41]. Furthermore, their poor electrical conductivity and weak charge storage capacity restrict the output power and efficiency of TENGs [42–45]. To address these limitations, simple yet effective processing strategies are required to enhance both the mechanical and electrical properties of aerogels, thereby optimizing their performance for TENG fabrication and expanding their application in smart wearables.

In this study, we report the first all-aerogel TENG (AA-TENG) with superior elasticity, high output performance, and ultralow density by utilizing simple and effective freeze-drying strategies. The electrodes of the AA-TENG are constructed from highly elastic ($\geq$90 % height retention) and flexible cellulose/carbon nanotube (CNT) aerogel, fabricating using the twice freeze-drying method. The triboelectric layer is composed of PVDF-TrFE aerogel with exceptional triboelectric properties, prepared via a simple directional freeze-drying and compression process. Furthermore, the mechanism of β-phase content in PVDF aerogel on enhancing triboelectric performance is systematically verified through density functional theory (DFT) and experimental studies. Exploiting its superior performance, the AA-TENG is further utilized as an active triboelectric sensor (TES) for developing a self-powered wireless fencing strike analysis system that can accurately record the strike location and timing with a rapid response time of $<$ 60 ms, to assist in competition judgments. Employing the convolutional neural network (CNN) algorithm, three types of fencing strikes can be precisely classified (100 % accuracy and 0.0858 loss of validation), offering valuable insights for improving accuracy and identifying weaknesses during training. This work provides novel strategies for self-powered systems in intelligent sports and big data analysis, with the potential for significant impact on the global sports industry.

2. Results

Smart wearable sports equipment enabled by the AA-TENG. By leveraging the low density of aerogels and the self-powered sensing capability of TENGs, the high elasticity and lightweight all-aerogel TENG can function as a self-powered biomechanical sensor. This combination ensures accurate data collection while minimizing interference with athletic performance, making it highly suitable for intelligent sports applications. Taking fencing as an example, the conceptual schematic of the smart fencing suit, illustrated in Fig. 1a, shows AA-TENGs distributed across the athlete's body. With its high elasticity, ultra-lightweight nature, and exceptional sensitivity, the system captures fencing strike signals in real time, facilitating accurate sensing and data monitoring. This technology not only helps reduce misjudgments in competitions but also assists athletes in refining their precision and accuracy during training. The exploded view of the AA-TENG shown in Fig. 1b reveals that the upper and lower substrates are composed of fencing suit fabric. While the intermediate cellulose/CNT aerogel electrodes provide both electrical conductivity and enhanced resilience compared to conventional aerogels. These electrodes effectively respond to pressure variations, serving as the electrode layer of the TENG. The middle friction layer consists of a PVDF-TrFE aerogel (PTA) through simple directional freeze-drying and compression, which exhibits significantly improved triboelectric performance compared to traditionally treated methods. In addition, Figs. 1c and 1d demonstrate the processibility of both cellulose/CNT aerogel and PVDF-TrFE aerogel, which can be prepared according to actual needs to meet diverse

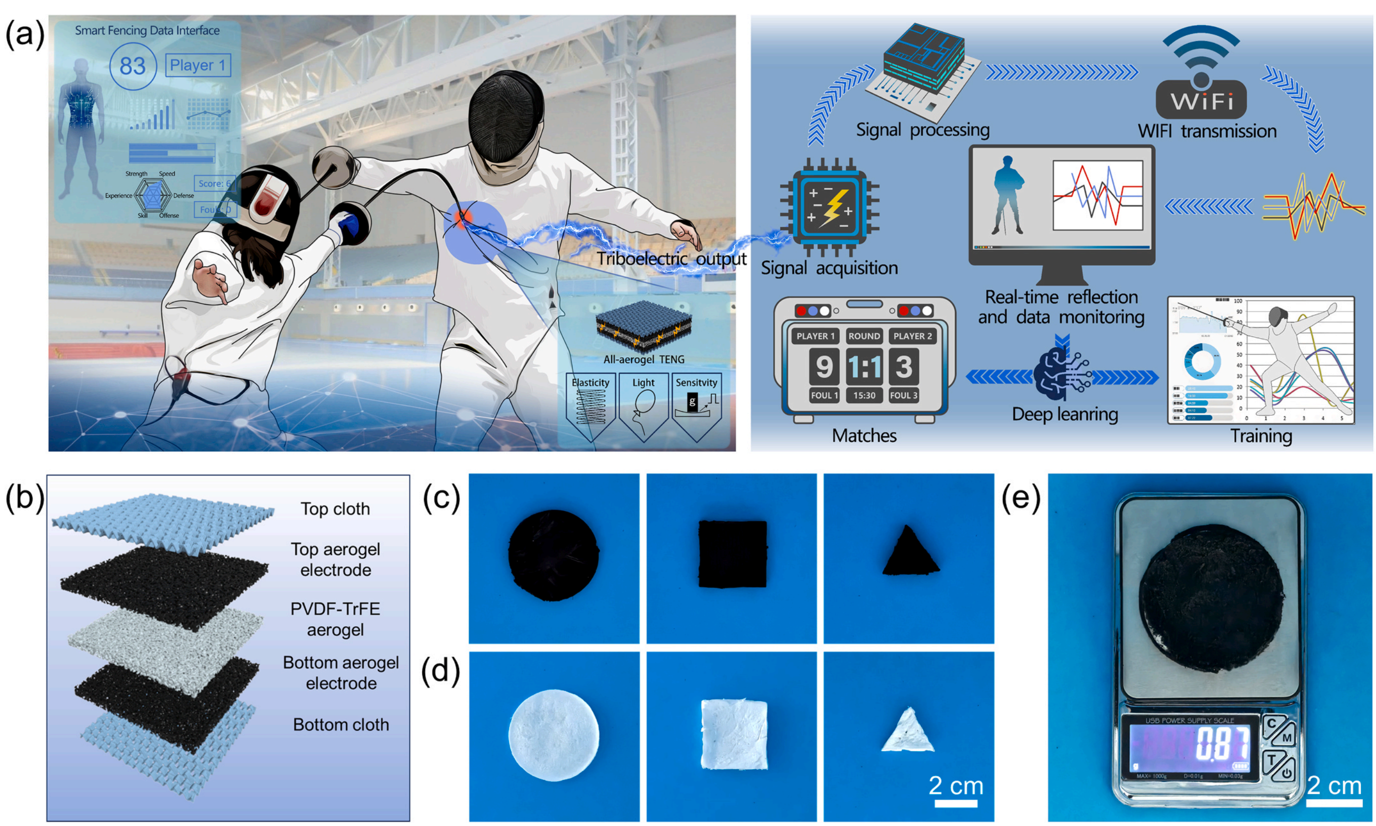

Fig. 1. Structure design and schematic of the AA-TENG. (a) Overview of the self-powered smart sensors installed on fencing suits for real-time sensing and data monitoring to assist matches and training. (b) Exploded view of structure design of the AA-TENG. Photographs of (c) cellulose/CNT aerogels and (d) PVDF-TrFE aerogels with different shapes. (e) Weight of the AA-TENG device.

application scenarios and specific functional requirements. As shown in Fig. 1e, the overall device density of the AA-TENG is only 7.92×10^{-3} g/cm^3, fully highlighting its ultra-lightweight nature.

Cellulose/CNT aerogel treatment and characterization. Cellulose is the most abundant natural polymer on Earth [46]. Its inherent biocompatibility and excellent processability make it suitable for diverse applications in energy and wearable technologies [47,48]. However, its mechanical durability requires improvement to ensure sustained operational reliability as a friction layer in TENG. Fig. 2a illustrates the preparation process of the cellulose/CNT aerogel. Natural wood undergoes chemical treatment to remove lignin and hemicellulose, followed by TEMPO oxidation to produce carboxylated cellulose nanofibers (CNFs). The resulting short-chain CNFs (Figure S1, Supporting Information) were subjected to a twice freeze-drying process to construct a hierarchical conductive aerogel. During the first directional freeze-drying step at −196 °C, CNFs assemble into sub-micron fibers (SMFs) with thick and long chains (Figure S2, Supporting Information), forming a cobweb-like porous skeleton. During the second freeze-drying process at −20 °C, carboxylated CNTs were integrated into SMFs via hydrogen bonding between their surface carboxyl groups and oxidized cellulose, yielding a cross-linked conductive network. To understand the mechanism underlying the aerogel's superelasticity, scanning electron microscope (SEM) was used to investigate its microstructure. As shown in Figure S3 (Supporting Information), the CNF aerogel exhibits a honeycomb-like structure with densely pore walls, resulting in high rigidity and low elasticity, which limits its effectiveness as a pressure sensor material. In contrast, the SMF aerogel presents a cobweb-like structure (Figure S4, Supporting Information). Moreover, the individual fibers are thicker and longer, with widths reaching several hundred nanometers and lengths at the micrometer scale (Fig. 2b, Figure S5, Supporting Information). This unique architecture enhances compressibility and resilience, enabling superior deformation recovery under pressure. When carboxylated CNTs are incorporated into the SMF dispersion, hydrogen bonds form between the carboxyl groups on CNTs and the carboxyl and hydroxyl groups on cellulose, facilitating the uniform dispersion of CNTs within the SMF network. As illustrated in Fig. 2c, this cross-linked structure forms a continuous conductive network, ensuring efficient electrical performance.

Fig. 2d displays the Fourier transform infrared (FTIR) spectra of cellulose and cellulose/CNT. The characteristic vibrational bands of SMF appeared at 3413, 2890, 1616, 1421, 1367, 1060, and 895 cm^{-1}, corresponding to the stretching of O-H groups, the asymmetrical stretching of aliphatic C-H units in pyranose rings, the C=O bonds of the carboxylic acid groups, the symmetric bending of -CH_2 units of pyranose rings, O-H bending, C-O-C pyranose ring skeletal vibrations, and C_1-H deformation vibrations, respectively [49]. Following the incorporation of CNTs, the FTIR spectrum of the cellulose/CNT blend retains the typical characteristic peaks of SMF, while the bands at 1616 cm^{-1} and 1421 cm^{-1}, originally attributed to carboxylated CNTs, shift to higher frequencies [50]. This shift suggests the presence of non-covalent interactions between CNTs and SMFs, likely due to hydrogen bonding and van der Waals forces, contributing to the aerogel's enhanced structural integrity and uniform dispersion.

To evaluate the thermal insulation performance of the cellulose/CNT aerogel, the conductive aerogel with a diameter of 50 mm and a thickness of 5 mm was placed on a 160 °C hot plate, and its temperature variation was recorded using an infrared thermal imaging camera. The corresponding infrared images and temperature-time curves are shown in Figs. 2e and 2f, respectively. The results indicate that the aerogel's highly porous structure effectively reduces heat conduction, maintaining good thermal insulation even at elevated temperatures. When incorporated into sportswear, this property helps minimize body heat loss and enhance wearer comfort, particularly in demanding environments. Besides that, the mechanical characteristics of aerogel play a vital role in sensor applications. The compression performance test (Fig. 2g, Figure S6, Supporting Information) demonstrates that the cellulose/CNT aerogel recovers its original shape after the removal of a 500 g load, with height retention of ~98 %, highlighting its excellent elasticity. The stress-strain curve further reveals that the cellulose/CNT aerogel exhibits remarkable compressibility, with minimal height loss under strains below 50 % (Fig. 2h). A comparative analysis of SMF aerogel is provided in Figure S7 (Supporting Information). Fig. 2i shows height retention under different strains, indicating that the cellulose/CNT aerogel maintains over 90 % height retention at strains ≤ 50 %. In addition, the cellulose/CNT aerogel exhibits notable anti-fatigue properties, as demonstrated by its ability to withstand 50 cyclic compressions at 50 % strain, confirming its superior deformation recovery (Fig. 2j). This performance surpasses that of SMF aerogel (Figure S8, Supporting Information), making it a highly resilient material suitable for long-term use in wearable sensor applications.

2.1. PVDF-TrFE aerogel treatment and characterization

Poly(vinylidene fluoride) (PVDF) and its copolymers exhibit high dielectric constants and electroactive properties [51–53], making them widely applicable in electronics and biomedical engineering [54]. However, conventional methods for enhancing β-phase content, such as solution processing [55], stretching [56], annealing [57], electric field polarization [58], often involve complex procedures and high production costs. To address these challenges, a simple, low-cost fabrication strategy was developed, achieving a β-phase content of 88.95 %, thereby significantly enhancing triboelectric performance. As illustrated in Fig. 3a, α-phase PVDF-TrFE powder (PTP) was dissolved in dimethyl sulfoxide (DMSO) solution and subsequently subjected to directional freeze-drying with liquid nitrogen. During this process, PVDF-TrFE underwent a phase transformation from the α-phase to the β-phase, ultimately forming a white and flexible β-phase PVDF-TrFE aerogel (Figure S9, Supporting Information). The SEM image of resulting aerogel reveals a 3D porous network with interconnected pores, a structure that contributes to its enhanced mechanical flexibility and dielectric properties (Fig. 3b).

To confirm that the primary phase transition in PVDF-TrFE during the freeze-drying process is the α-to-β phase transformation, a comparative analysis was conducted on PVDF-TrFE after hot-pressing (PTHP), the freeze-dried PVDF-TrFE aerogel, and the PVDF-TrFE aerogel after pressing (PTAP). As shown in Fig. 3c, FTIR spectroscopy was used to analyze the phase composition of the samples. For PTP, distinct α-phase peaks were observed at 614, 766, 795, and 976 cm^{-1}, with a weak β-phase absorption peak at 840 cm^{-1}, confirming that PTP primarily consists of the α-phase. Similarly, PTHP displayed an increased absorption intensity at 840 cm^{-1}, indicating a partial β-phase increase, though it remained predominantly α-phase. In contrast, PTA and PTAP exhibited significant spectral shifts, with strong absorption peaks at 510, 840, and 1279 cm^{-1}, characteristic of the β-phase, confirming a dominant phase transformation. According to Sencadas et al. [59], it was assumed that the FTIR absorption follows the Lambert-Beer law. Based on this assumption, the absorption coefficients K at wavenumbers of 766 and 840 cm^{-1} were calculated respectively. Thus, the relative proportion of the β-phase in PVDF samples can be determined using the following equation:

$$F(\beta) = \frac{A_{\alpha}}{\left(\frac{K_{\beta}}{K_{\alpha}}\right)A_{\alpha} + A_{\beta}}$$

Here, F(β) represents the content of the β-phase; the absorbances of A_α and A_β are at 766 and 840 cm^{-1} respectively; K is the absorption coefficient at the respective wavenumbers, which are 6.1×10^4 and 7.7×10^4 cm^2 mol^{-1} respectively. The calculated β-phase content for each sample is shown in Figure S10 (Supporting Information), revealing that the β-phase content of PTAP reaches 88.95 %, demonstrating a significant enhancement.

As illustrated in Fig. 3d, the XRD analysis further confirmed these

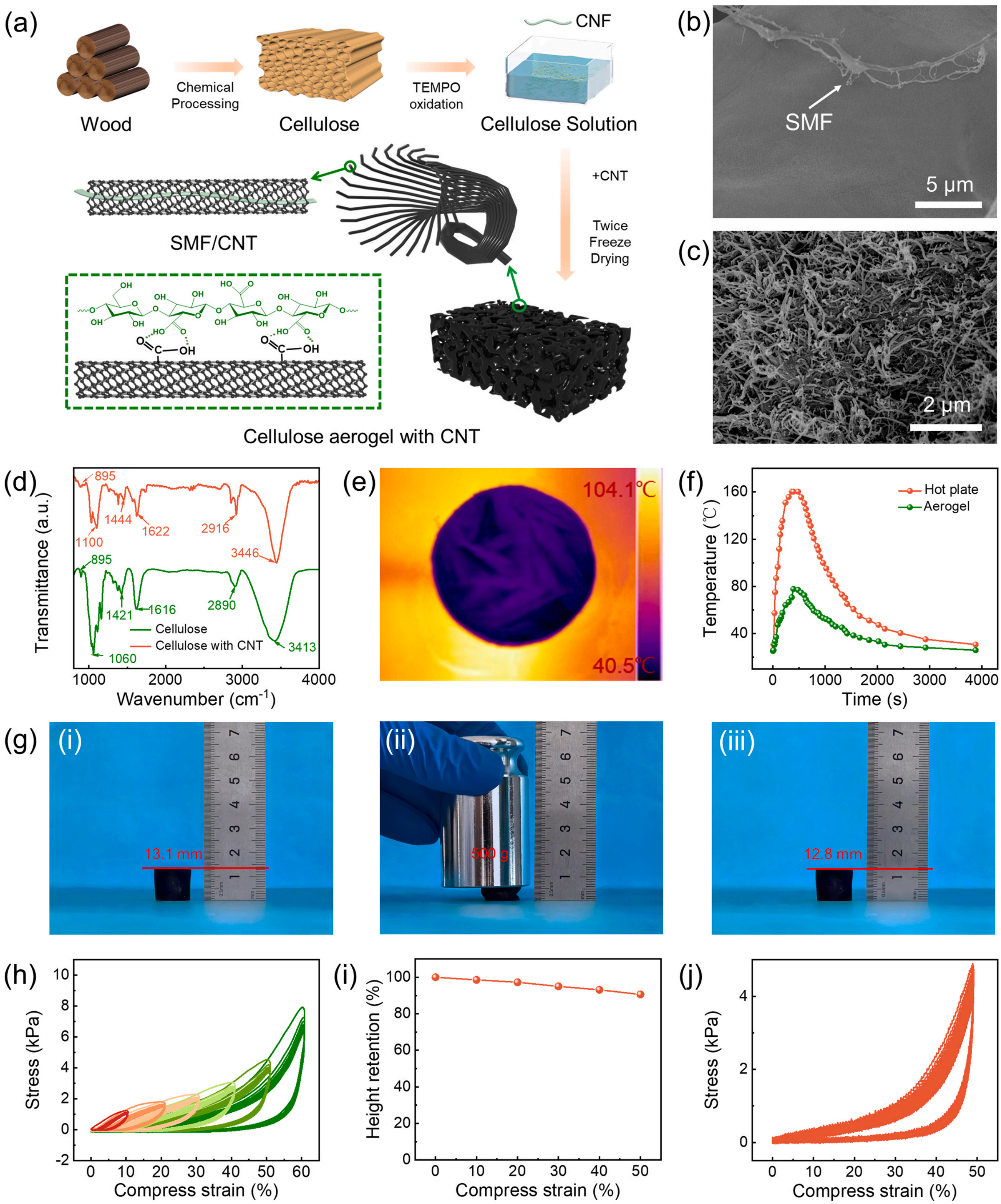

Fig. 2. Fabrication and characterization of the Cellulose/CNT aerogel. (a) Diagram of the process for fabricating the cellulose/CNT aerogel. Scanning electron microscopy (SEM) image of (b) SMF aerogel and (c) cellulose/CNT aerogel. (d) FTIR spectra of cellulose and cellulose/CNT aerogels. (e) Thermal infrared images of cellulose/CNT aerogel at 100 ℃. (f) Temperature-time curves of cellulose/CNT at 160 ℃. (g) Photographs demonstrating cellulose/CNT aerogel before and after compression by a 500 g weight. (h) Compressive stress-strain curves of cellulose/CNT aerogel at strains from 10 % to 60 %. (i) Height retention of cellulose/CNT aerogel at strains from 0 % to 50 %. (j) Cyclic compressive stress-strain curves of cellulose/CNT aerogel at 50 % strain.

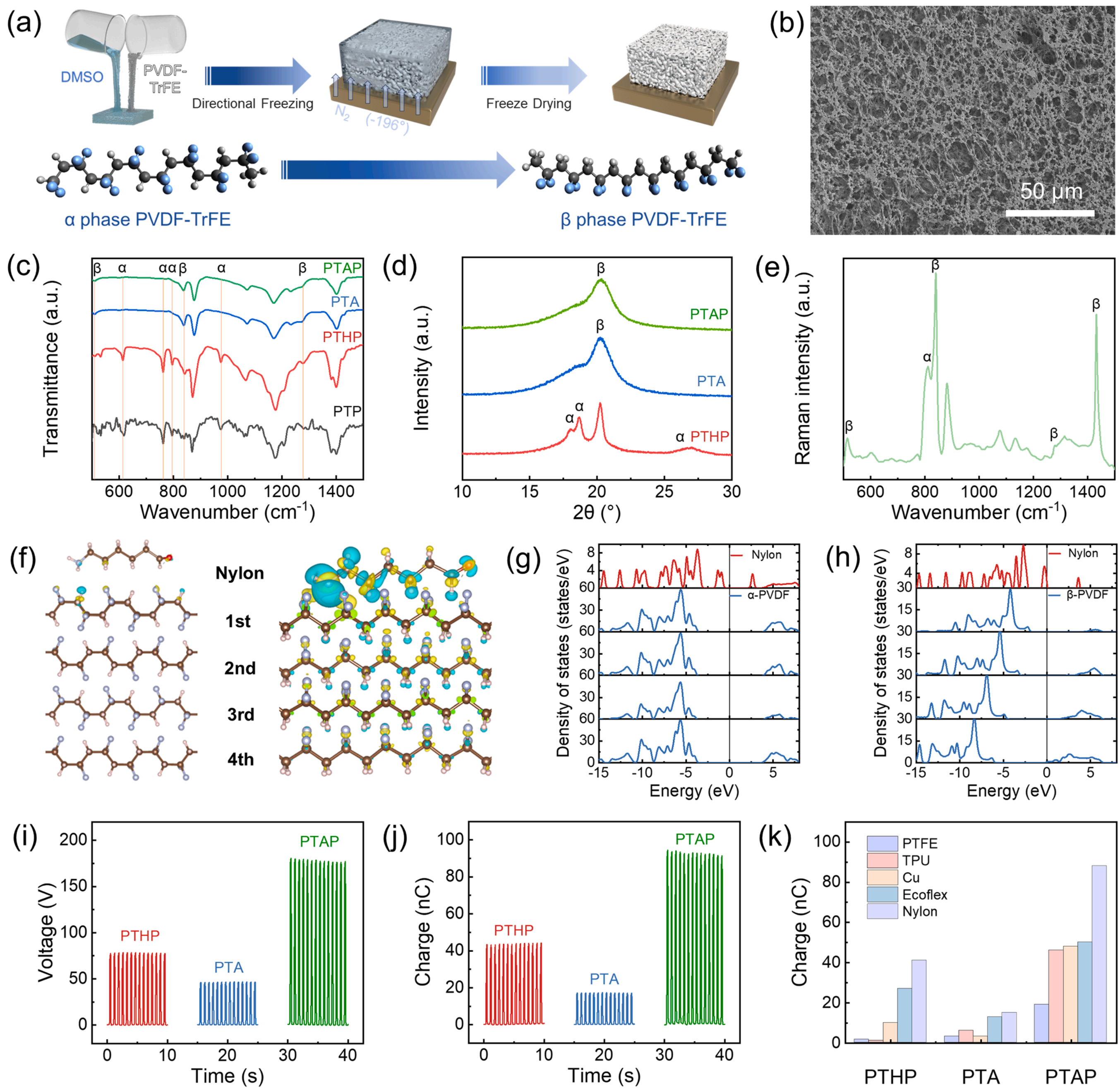

Fig. 3. Fabrication and characterization of the PVDF-TrFE aerogel. (a) Fabrication steps of PVDF-TrFE aerogel. (b) SEM image of PVDF-TrFE aerogel film surface. (c) FTIR image of PVDF-TrFE powder (PTP), PVDF-TrFE after hot-pressing (PTHP), PVDF-TrFE aerogel (PTA), and PVDF-TrFE aerogel after pressing (PTAP). (d) XRD image of PTHP, PTA, and PTAP. (e) Raman spectra of PTAP. (f) Charge density difference for Nylon/α-PVDF and Nylon/β-PVDF contact interface. The layer-dependent density of states for the (g) Nylon/α-PVDF and (h) Nylon/β-PVDF contact interface. (i) The voltage and (j) charge output of PTHP, PTA, and PTAP with Nylon-6. (k) The charge output of PTHP, PTA, and PTAP with Nylon, Cu, ecoflex, TPU, and PTFE.

findings. PTP and PTHP exhibited α-phase diffraction peaks at 18.00° (100), 18.6° (020), and 27.04° (021), alongside a minor β-phase peak at 20.2° (110). In contrast, PTA and PTAP displayed only a β-phase peak at 20.26° (110) (200), confirming a complete phase transformation. The Raman spectrum reinforced these results, with PTAP exhibiting dominant β-phase absorption bands at 509, 840, 1275, and 1442 cm^{-1}, while only weak α-phase peaks were observed at 604 and 810 cm^{-1} (Fig. 3e). Collectively, FTIR, XRD, and Raman spectroscopy analyses confirm that PVDF-TrFE, when processed using DMSO as the solvent and subjected to directional freeze-drying, undergoes a substantial phase transformation from α-phase to the β-phase, demonstrating the effectiveness of the freeze-drying method in enhancing the electroactive properties of PVDF-TrFE.

To theoretically validate that increasing the β-phase content in PVDF materials enhances their triboelectric performance, we performed DFT calculations for PVDF/Nylon contact interface with different phases and analyzed charge transfer between PVDF and Nylon, as schematically shown in Fig. 3f. The calculated results indicate that when Nylon interacts with α-phase PVDF, charge transfer is limited to the surface of the PVDF. In contrast, when Nylon contacts with β-phase PVDF, charge transfer occurs both on the surface and within the polymers. This indicates that the β-PVDF exhibits a greater charge transfer than α-PVDF, leading to enhanced triboelectric charge generation during the friction process. This enhanced charge transfer is attributed to its relatively large built-in electric field, which facilitates electron transfer at the interface upon contact with Nylon. Fig. 3g further supports this observation by illustrating the layer-resolved density of states in different layers of α-phase PVDF. The uniformity of these band edges indicates the absence of a built-in electric field. Conversely, in the β-PVDF/Nylon system, the band edges shift layer-by-layer in β-PVDF, indicative of a pronounced built-in electric field (Fig. 3h). Similarly, the average electrostatic potential distributions of PVDF/Nylon contact models, shown in Figure S11 (Supporting Information), provide similar evidence. The α-PVDF/Nylon contact interface results in a relatively uniform

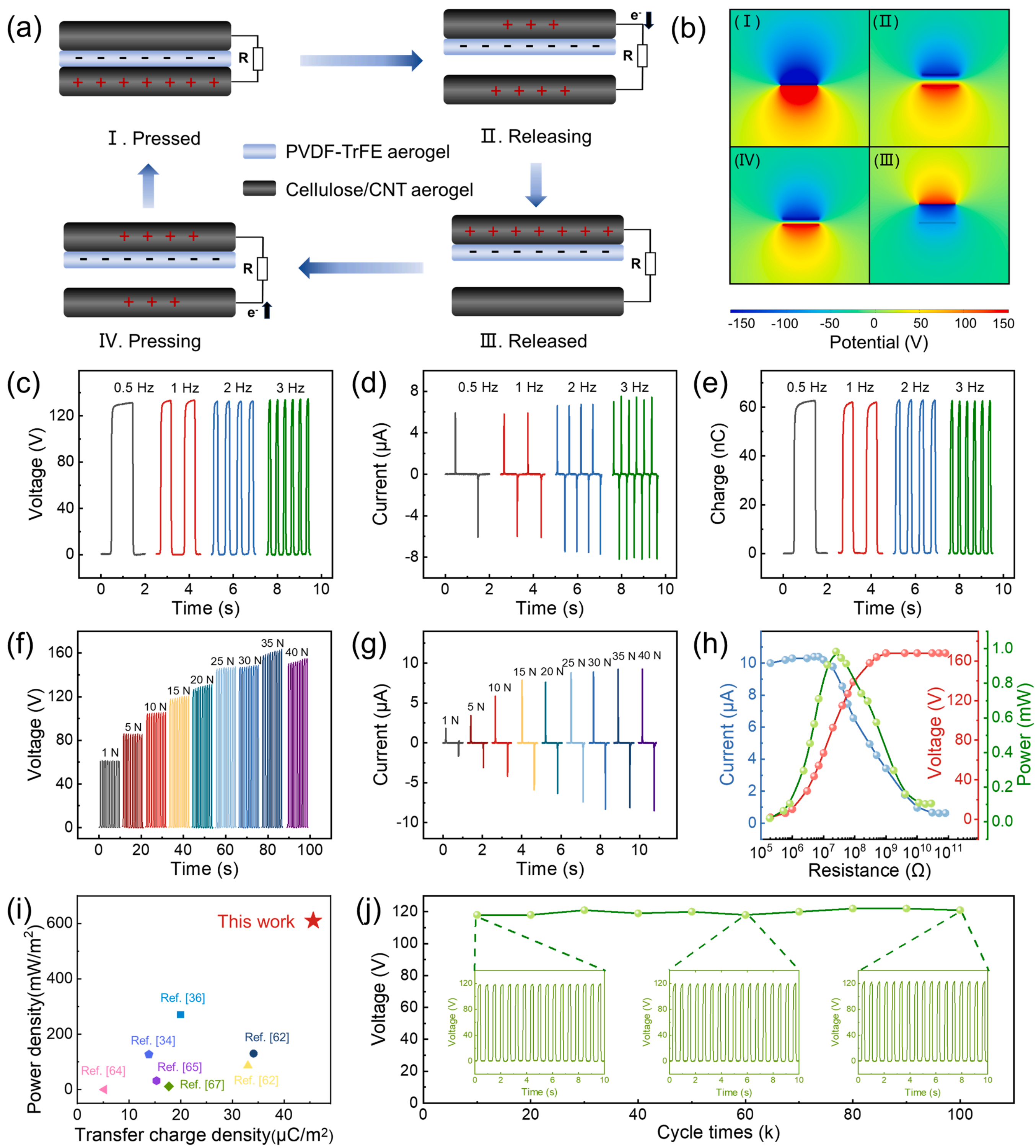

Fig. 4. Working principle and electrical output performance of the AA-TENG. (a) Working mechanism of the AA-TENG under vertical contact-separation mode. (b) Potential simulation by COMSOL to elucidate the working principle. (c) Open-circuit voltage, (d) short-circuit current, and (e) transferred charge of the TENG with various pressing frequencies. (f) Open-circuit voltage and (g) short-circuit current of the TENG with different applied forces. (h) Peak power density, measured output current and voltage on different external loading resistances. (i) Comparison of the power density and transfer charge density of aerogel-based TENGs obtained in this work with results reported in the literature. (j) Stability and robustness measurement of the AA-TENG, where the output voltage was recorded for over 100,000 cycles at a frequency of 2 Hz.

electrostatic potential distribution, implying the lack of a built-in electric field, while β-PVDF/Nylon contact interface exhibits a distinct potential gradient ("tilted" profile), clearly manifesting the presence of a significant built-in electric field. This alteration could reduce the depth of the potential well for electrons on the Nylon surface, thereby lowering the interface barrier and facilitating electron transfer [60].

To experimentally verify the triboelectric property enhancement of PVDF by improving β-phase content, output performances of TENGs with "Nylon-various PVDF" triboelectric pairs in contact-separation mode are compared. As shown in Fig. 3i, the output voltage of TENG based on PTAP reaches 180 V, which is 57 % higher than that of the PTHP. Considering that the PTAP and PTHP are in the same thickness, this output power enhancement can be attributed to the improvement of β-phase content. When using PTA for fabricating TENG, the output voltage is only 45 V, which is due to its excessive thickness for reducing the electrostatic induction. The output charge and current of the TENGs based on various PVDF-TrFE samples also show similar trends (Fig. 3j, Figure S12, Supporting Information). When in contact with different materials, the charge output of TENGs based on various PVDF-TrFE samples is summarized in Fig. 3k. These results confirm that using DMSO as the solvent in the directional freeze-drying process with liquid nitrogen provides a simple, rapid, and efficient approach for fabricating PVDF-TrFE aerogels with high β-phase content and enhanced triboelectric performance.

2.2. Output performance of the AA-TENG

Considering the excellent mechanical and triboelectric properties of the cellulose/CNT and PVDF-TrFE aerogels, we further fabricated the highly elastic, lightweight, and high-performance AA-TENG by utilizing them as electrode and friction layer. The working principle of the AA-TENG is illustrated in Fig. 4a. The relative motion during one operational cycle can be simplified as a contact-separation process between the two layers. When the PTAP comes into contact with the bottom cellulose/CNT aerogel, interfacial electrification occurs, generating equal amounts of opposite charges on the surfaces of the PTAP and the cellulose/CNT aerogel, respectively (State I). Due to its higher electron affinity, the PTAP becomes negatively charged compared to the cellulose/CNT aerogel. At this stage, the opposing charges are aligned in close proximity, resulting in a negligible electrical potential difference between the two surfaces. As the surfaces begin to separate, electrostatic induction drives the transfer of positive charges from the bottom electrode to the top electrode (State II). At maximum separation, the negative triboelectric charges on the PTAP are fully balanced by the induced positive charges in the top electrode (State III). Notably, the accumulated charges are preserved over an extended period due to the insulating properties of the materials. During the re-approach phase, the accumulated positive charges in the top electrode flow back to the bottom electrode through the external load, compensating for the potential difference (State IV). Upon re-establishing contact (State I), the negative charges on the PTAP are neutralized by the positive charges on the bottom electrode. Consequently, each contact-separation cycle of the SI-TENG produces an alternating potential and current across the external load. A theoretical analysis on the AA-TENG was conducted using the finite element method in COMSOL software (Fig. 4b). The simulation results indicated that the potential distribution changes with the spacing between the triboelectric layers, corroborating the theoretical predictions and experimental findings.

The output performance of the AA-TENG was evaluated using a computer-controlled linear motor to simulate various compression motions. All the tests were carried out using TENG devices with a size of 4×4 cm. The open-circuit voltage, short-circuit current, and transferred charge with different frequencies are shown in Fig. 4c-e. At a contact-separation distance of 30 mm with the applied force of 20 N, the open-circuit voltage and transferred charge remained constant at approximately 130 V and 62 nC across frequencies ranging from 0.5 to 3 Hz. Meanwhile, the short-circuit current increased from 6 μA at 0.5 Hz to 8 μA at 3 Hz, suggesting that higher frequencies enhance current generation. This is attributed to the constant transferred charge under varying frequencies, where an increased frequency leads to a higher charge transfer rate, resulting in a higher current output. Subsequently, the influence of different external forces on the output performance of AA-TENG was investigated. A force gauge was employed to measure the applied force while maintaining a frequency of 1 Hz and a contact-separation distance of 30 mm. As shown in Fig. 4f, an initial applied force of 1 N resulted in an output voltage of 60 V. With increasing applied force, the output voltage progressively rose, reaching a maximum of 160 V at 35 N. Similarly, the short-circuit current increased from 1.8 μA at 1 N to 9.2 μA at 40 N (Fig. 4g). As shown in Figure S13 (Supporting Information), the transferred charge also increased with applied force, which could be due to improved contact between the triboelectric layers. The output performance of the AA-TENG exhibited only minor fluctuations within the extended pressure range from 35 N to 60 N, maintaining stable performance characteristics (Figure S14, Supporting Information). The use of aerogel materials in all TENG components can enhance pressure sensitivity, making it well-suited for pressure-sensing applications. As pressure increases, the AA-TENG undergoes deformation, and the porous aerogel structure increases the effective contact area, further improving electrical output performance.

To evaluate the effective output power of the AA-TENG, the output voltage was measured under varying external load resistances at a working frequency of 1 Hz and an applied force of 35 N. The relationship between the output voltage/power and the resistor is shown in Fig. 4h. At the external load resistor of 40 MΩ, the maximum peak output power reached 0.98 mW, corresponding to an areal power density of 0.61 W m^{-2}. Benefiting from the high β-phase content of the PVDF-TrFE aerogel, the output performance of the AA-TENG device was higher than that of other aerogel-based TENGs previously reported (Fig. 4i) [37,39,58,61–64]. Additionally, the charging performance of the AA-TENG with different capacitors is presented in Figure S15 (Supporting Information). As depicted in Fig. 4j, when operated at a working frequency of 2 Hz with a contact distance of 30 mm, while the applied force was 15 N, the open-circuit voltage remained stable at 120 V, exhibiting no noticeable attenuation even after 100,000 continuous cycles, demonstrating its excellent stability. Figure S16 (Supporting Information) further highlights the pressure-dependent sensitivity of the AA-TENG, revealing a triphasic linear response. The device exhibits a high sensitivity of 3.49 V/N within the 0–20 N pressure range. As shown in Figure S17 (Supporting Information), the response time of this self-powered sensor is less than 60 ms. Given its exceptional mechanical and triboelectric performance, the AA-TENG is highly suitable for self-powered pressure sensing in sports equipment. Its integration into intelligent sports systems can facilitate real-time data collection and analysis, thereby providing valuable insights for athletic training and competition monitoring.

2.3. Self-powered wireless fencing strike analysis system

With the advancement of modern fencing, increasing demands have been placed on athletes' skill levels, particularly in strike accuracy, which plays a critical role in determining competition outcomes. To enhance training quality, competition flexibility, and simplify sports equipment, a self-powered wireless fencing strike analysis system was developed based on the AA-TENG. This system converts pressure variations induced by fencing strikes into electrical signals, providing real-time feedback on competition dynamics. Under such circumstances, the AA-TENG operates as a self-powered TES for sensing and analysis. As a proof-of-concept demonstration, a 2×4 TES array was fabricated and embedded beneath the fencing suit to detect hit signals (Figure S18, Supporting Information). The size of each AA-TES unit is about 7 cm^2, and the entire fencing model is shown in Figure S19 (Supporting Information). The wireless multi-channel acquisition module for the self-powered system is illustrated in Figure S20 (Supporting Information). As shown in Fig. 5a, when the sword hits the target, the AA-TES at the hit position will generate a distinct output signal. Through the multi-channel data acquisition method, the real-time voltage signals of each sensor unit can be captured simultaneously. Once processed, the statistical results are displayed within the program interface. Fig. 5b presents an overview of the self-powered fencing strike analysis system, with an enlarged view shown in Fig. 5c, including the array distribution diagram, the real-time array voltage diagram, the hit number statistics chart, the timer, the round counter, and the real-time voltage signals of each channel. For demonstration purposes, training swords were used to repeatedly strike the fencing display model. Each strike generated a unique signal pattern, immediately displayed on the array voltage diagram, while the hit count for each unit was recorded (Video S1, Supporting Information). These results confirm the system's high accuracy in detecting hit patterns and tracking hit distribution.

Supplementary material related to this article can be found online

Based on fencing regulations, hit patterns were classified into three categories: thrust, miss (hitting outside the valid area), and whip. Fig. 5d illustrates the output signal profiles of these three hit types, highlighting distinct variations between them, with additional details provided in Videos S2 and S3 (Supporting Information). Thrusting, where the tip of the sword makes direct contact with the target, is the primary scoring method in fencing. Fig. 5e provides the enlarged view of the thrusting signal, with a photo of a thrusting hit displayed in the upper right corner. The precise impact time of the first strike was recorded at 0.56 s, with accuracy dependent on the signal sampling rate. Compared to traditional lighting-based scoring systems, this method offers greater accuracy, objectivity, and fairness. Fig. 5f presents the enlarged view of the missed signal, with an image of a strike outside the valid scoring area in the upper right corner. In fencing competitions, the valid scoring zones vary depending on the event, necessitating precise hit validation. Tracking missed hits reveals accuracy gaps. For example, a foil strike on the shoulder (a non-scoring area) generates a near-standby signal intensity, enabling real-time feedback to refine targeting strategies during training. Fig. 5g illustrates an enlarged view of the whipping signal, with a photo of a whipping hit in the upper right corner. Unlike thrusting, whipping involves the sword body contacting the target rather than just the tip. This technique is recognized as a valid scoring method only in saber fencing, making it crucial to accurately identify whipping signals. Unlike thrusting or missed hits, whipping signals activate multiple sensor units simultaneously, enabling strike trajectory reconstruction through temporal signal analysis. This sensor-driven approach outperforms video-based methods by delivering millisecond-level strike path quantification, providing real-time actionable feedback for precision training and objective competition assessment.

Supplementary material related to this article can be found online

Fencing's rapid strike exchanges make real-time judgment difficult. Current high-speed camera verification is costly and lacks real-time feedback, while manual analysis of sensor data further complicates real-time decision-making, reducing efficiency and accuracy. To overcome these limitations, deep-learning techniques can be employed to analyze the voltage signals generated by the AA-TENG during thrusting, missed hits, and whipping strikes. These techniques enable the identification of signal patterns and distinctions by autonomously learning from large datasets of characteristic parameters. For the classification of voltage signals, a Convolutional Neural Network (CNN)-based deep-learning model was designed and implemented, as illustrated in Fig. 5h. The model follows a structured pipeline of data acquisition, feature extraction, network construction, and signal classification to effectively categorize three strike types: thrust, miss, and whip. During experimental testing, fencing actions were repeatedly performed to collect sufficient data, with 240 data groups allocated for model training and 60 for testing. Fig. 5i presents the confusion matrix of the CNN classification results for the three striking techniques. Over 200 training epochs, the model exhibited stable convergence, achieving 100 % validation accuracy at the 197th epoch, with a minimum validation loss of 0.0673 (Figure S21, Supporting Information). These results confirm the model's high classification accuracy and robustness. This study integrates AA-TES technology to convert key mechanical information in fencing into electrical signals, leveraging deep learning for precise, real-time data interpretation. This achievement has significant implications for fencing, offering precise feedback in training, facilitating personalized training programs, assisting referees in ensuring fair play, and optimizing competition strategies.

3. Conclusion

In conclusion, we have developed a highly elastic, lightweight, and high-performance AA-TENG for self-powered sensing in intelligent fencing training. The AA-TENG features electrodes composed of a highly elastic cellulose/CNT aerogel (≥90 % height retention) fabricated via a twice freeze-drying method, paired with a triboelectric layer of PVDF-TrFE aerogel (β-phase content: 88.95 %) prepared through a directional freeze-drying and compression process. This innovative approach enhances the output performance by 57 % compared to conventional methods. The resulting AA-TENG exhibits an ultralow density of 7.92×10^{-3} g/cm^3. Leveraging its exceptional performance, the AA-TENG was employed as an active triboelectric sensor in a self-powered wireless fencing strike analysis system, capable of accurately detecting strike locations and timing with a rapid response time (<60 ms), thereby aiding in competition judgments. By integrating a CNN algorithm, the system achieved precise classification of three fencing strike types with 100 % accuracy and a validation loss of 0.0673, providing valuable insights for performance enhancement and weakness identification during training. This study not only demonstrates the novel application of TENGs in athletic analytics but also paves the way for the development of aerogel-based electronics by combining self-powered systems with deep learning, offering significant potential for advancements in athletic big data analytics.

4. Experimental section

4.1. Materials and chemicals

Cellulose was extracted from eucalyptus wood. Sodium hydroxide (> 97 %, Sigma-Aldrich), sodium hypochlorite (6–14 % active chlorine basis, Aladdin), acetic acid (99.5 %, Aladdin), 2,2,6,6-tetramethylpiperidine-1-oxyl (≥98 %, Aladdin), sodium bromide (≥99 %, Aladdin), carboxylated multiwalled carbon nanotubes aqueous dispersionand (carbon nanotube content: ≈10 wt%, XFNANO) and deionized (DI) water were used for processing the cellulose/CNT aerogel. Dimethyl sulfoxide (≥99.9 %, Aladdin) and PVDF-TrFE (powder with the TrFE molar ratio of 30 %, Akema) were used for processing the PVDF-TrFE aerogel.

4.2. Preparation of SMF/CNT conductive aerogel

Eucalyptus wood was first crushed and sieved to obtain fine wood powder. The sieved powder was then immersed in an aqueous solution of sodium hypochlorite and glacial acetic acid (with a volume ratio of 1:1), and heated under continuous stirring. The reaction was considered complete when the wood powder transitioned from brownish-yellow to white. The precipitate was then repeatedly washed with distilled water until the pH reached 7. Next, the purified precipitate was treated with a 4 wt% sodium hydroxide solution, heated, and stirred for 6 hours. The resulting cellulose was thoroughly washed with distilled water until a neutral pH (pH 7) was achieved, yielding purified wood-derived cellulose. The extracted cellulose was subsequently subjected to TEMPO oxidation to obtain carboxylated cellulose. A 0.5 wt% solution of carboxylated cellulose was directionally frozen using liquid nitrogen at −196 °C and freeze-dried for 48 hours to yield SMF cellulose. The

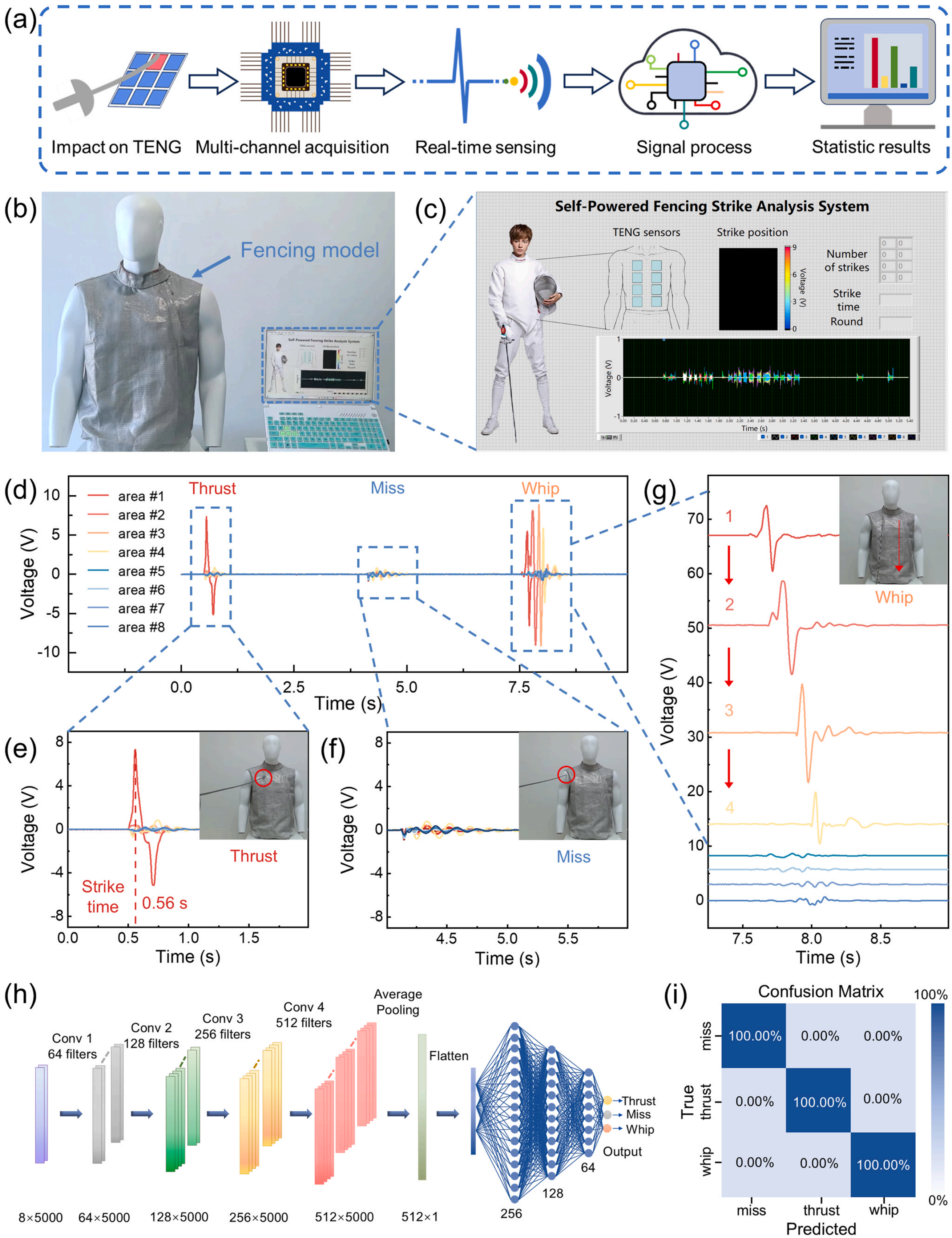

Fig. 5. Application of the AA-TENG in a self-powered wireless fencing strike analysis system. (a) Scheme diagram of the AA-TENG-based self-powered wireless fencing strike analysis system. (b) Photograph of the application scenarios of AA-TENG sensors for self-powered fencing strike analysis system. (c) Screenshot showing the real-time statistical result of the self-powered system. (d) Real-time signals from smart fencing cloth under the different hit patterns. (e) thrust signal, (f) miss signal and (g) whip signal. (h) Schematics of the process and parameters for constructing the 1D CNN structure. (i) Confusion matrix of test results.

obtained SMF was then redispersed in distilled water and further processed using an ultrasonic cell disruptor in an ice bath to ensure uniform dispersion. Carboxylated CNTs were then mixed with the SMF at a mass ratio of 1:2. The resulting mixture was placed in a −50 °C freezer and frozen overnight, followed by a 48-hour freeze-drying process to obtain the SMF/CNT conductive aerogel.

4.3. Preparation of PVDF-TrFE aerogel

PVDF-TrFE powder was dissolved in DMSO at a polymer concentration of 10 wt%. The solution was mechanically stirred at 70 °C for 8 hours to ensure complete dissolution. The resulting PVDF-TrFE solution was uniformly coated onto a template and immediately frozen upon deposition. The freezing process proceeded directionally from bottom to top. The sample was then placed in a −50 °C refrigerator overnight to ensure complete solvent crystallization. Following the freezing step, the sample was immersed in a deionized water bath to remove residual DMSO, a process repeated four times to ensure thorough solvent extraction. After DMSO removal, the sample was refrozen and subsequently freeze-dried for 25 hours to eliminate any remaining moisture. To obtain PTAP, the aerogel was compressed into a thin film using a hydraulic press. For comparison, PTHP was prepared using the conventional hot-pressing method.

4.4. Fabrication of the AA-TENG

The obtained SMF/CNT conductive aerogel and PVDF-TrFE aerogel were shaped into the desired forms to serve as the electrode and dielectric electrification layer, respectively, for constructing the contact-separation mode TENG. For the single-electrode mode TENG designed for fencing applications, the SMF/CNT conductive aerogel was attached to the inner side of the fencing uniform, while another SMF/CNT conductive aerogel, with a PVDF-TrFE aerogel layer on top, was affixed to the fencing model. Cu wires were connected to each SMF/CNT conductive aerogel to establish an electrical connection.

4.5. DFT calculations

First-principles calculation is performed using the projector-augmented wave method within the density-functional theory, as implemented in the Vienna Ab-initio Simulation Package (VASP). For the exchange-correlation energy, we implement the Becke three-parameter Lee-Yang-Parr hybrid function. To accurately describe intermolecular interaction, van der Waals correction is used. Our convergence standard requires that the Hellmann-Feynman force on each atom is less than 0.01 eV/Å and the absolute total energy difference between two successive consistent loops is smaller than 10^{-5} eV. The PVDF/Nylon contact interfaces are fully optimized using a Γ-centered $3 \times 3 \times 1$ k-grid, and the plane wave energy cutoff is set to 500 eV.

4.6. Characterization and measurements

The AA-TENG was driven by a linear motor (Linmot E1100) for electrical measurements. A programmable electrometer (Keithley 6514) was used to test the open-circuit voltage, short-circuit current and transferred charges. For multichannel voltage measurements of the triboelectric sensor array in the smart fencing cloth, a matched wireless multi-channel acquisition circuit (including a power management module, a 16-bit AD acquisition module, a pre-charge amplifier, an ESP32 WiFi module, and a STM32L431 main control chip) was used. The software platform was developed based on LabVIEW, which is capable of realizing real-time multi-channel data acquisition and analysis. A scanning electron microscope (SU8020, Hitachi) and a transmission electron microscope (Tecnai G20 20 TWIN UEM, FEI) were used to characterize the morphologies of the aerogel samples. An X-ray diffraction (X'pert3 Powder, Malvernpanalytical) was used to measure the XRD spectrum. A Raman microscope (LabRAM HR Evolution, Horiba JY) was used to measure the Raman spectroscopy. A Fourier transform infrared spectroscope spectrometer (VERTEX80v, Bruker) was used to measure the FTIR spectrum. Mechanical compression properties of the cellulose aerogel samples were measured using a E3000 fully electronic dynamic and static fatigue test system (Instron Limited). Compression tests were performed at 50 % strain with a cycle duration of 4 s per cycle, under the temperature of 24℃ and a relative humidity of 35 %.

CRediT authorship contribution statement

Chen Muqi: Writing – original draft, Investigation, Conceptualization. **Ji Minglan:** Writing – original draft, Investigation, Formal analysis. **Huang Lijun:** Visualization, Investigation. **Wu Ning:** Formal analysis. **Jiang Tao:** Visualization. **Li Chengyu:** Investigation. **Li Wanpeng:** Investigation. **Yu Boyang:** Visualization. **Luo Jianjun:** Writing – review & editing, Supervision, Funding acquisition, Conceptualization. **Li Xiaoyi:** Writing – review & editing, Supervision. **Wang Zhong Lin:** Writing – review & editing, Supervision, Funding acquisition.

Declaration of Competing Interest

The authors declare that they have no known competing financial interests or personal relationships that could have appeared to influence the work reported in this paper.

Acknowledgements

The research was supported by the National Natural Science Foundation of China (Grant No.52472307), National Key R & D Project from Minister of Science and Technology (2021YFA1201601, 2021YFA1201604), Shandong Provincial Natural Science Foundation (ZR2024YQ041), and Youth Innovation Promotion Association, CAS..

Appendix A. Supporting information

Supplementary data associated with this article can be found in the online version at doi:10.1016/j.mser.2025.101004.

Data availability

The data that support the findings of this study are available from the corresponding author upon reasonable request.

References

[1] R. Haight, W. Haensch, D. Friedman, Solar-powering the Internet of Things, Science 353 (2016) 124–125.
[2] L. Portilla, K. Loganathan, H. Faber, et al., Wirelessly powered large-area electronics for the Internet of Things, Nat. Electron. 6 (2023) 10–17.
[3] E. Landhuis, Neuroscience: big brain, big data, Nature 541 (2017) 559–561.
[4] V. Marx, The big challenges of big data, Nature 498 (2013) 255–260.
[5] J. Luo, Z. Wang, L. Xu, et al., Flexible and durable wood-based triboelectric nanogenerators for self-powered sensing in athletic big data analytics, Nat. Commun. 10 (2019) 5147.
[6] Q. Chen, D. Xu, Y. Yan, et al., A self-powered tennis training system based on micro-nano structured sensing yarn arrays, Adv. Funct. Mater. 35 (2025) 2414395.
[7] J. Luo, W. Gao, Z.L. Wang, The triboelectric nanogenerator as an innovative technology toward intelligent sports, Adv. Mater. 33 (2021) 2004178.
[8] Y. Zou, P. Tan, B. Shi, et al., A bionic stretchable nanogenerator for underwater sensing and energy harvesting, Nat. Commun. 10 (2019) 2695.
[9] Z. Liu, Y. Hu, X. Qu, et al., A self-powered intracardiac pacemaker in swine model, Nat. Commun. 15 (2024) 507.
[10] R.L. Bulathsinghala, W. Ding, R.D.I.G. Dharmasena, Triboelectric nanogenerators for wearable sensing applications: a system level analysis, Nano Energy 116 (2023) 108792.
[11] X. Li, M. Chen, R. Yu, et al., Enhancing light emission of ZnO-nanofilm/Si-micropillar heterostructure arrays by piezo-phototronic effect, Adv. Mater. 27 (2015) 4447–4453.

[12] J. Xu, X. Wei, R. Li, et al., Intelligent self-powered sensor based on triboelectric nanogenerator for take-off status monitoring in the sport of triple-jumping, Nano Res. 15 (2022) 6483–6489.
[13] S.-N. Lai, H.-T. Hsu, J.M. Wu, Smart ping-pong paddle with triboelectric self-powered wireless sensors, Nano Energy 131 (2024) 110158.
[14] D. Heo, J. Hur, S. Lee, et al., Commercial soccer ball-integrated triboelectric nanogenerator, Adv. Eng. Mater. 26 (2024) 2400134.
[15] H. Liu, J. Cao, S. Feng, et al., Highly sensitive and durable, triboelectric based self-powered nanosensor for boundary detection in sports event, Adv. Mater. Technol. 8 (2023) 2201766.
[16] J. Yuan, J. Xue, M. Liu, et al., Self-powered intelligent badminton racket for machine learning-enhanced real-time training monitoring, Nano Energy 132 (2024) 110377.
[17] C. Li, Z. Xu, S. Xu, et al., Miniaturized retractable thin-film sensor for wearable multifunctional respiratory monitoring, Nano Res. 16 (2023) 11846–11854.
[18] E. Aramendia, P.E. Brockway, P.G. Taylor, et al., Estimation of useful-stage energy returns on investment for fossil fuels and implications for renewable energy systems, Nat. Energy 9 (2024) 803–816.
[19] Y. Chen, H. Shen, G. Shen, et al., Substantial differences in source contributions to carbon emissions and health damage necessitate balanced synergistic control plans in China, Nat. Commun. 15 (2024) 5880.
[20] F.-R. Fan, Z.-Q. Tian, Z. Lin Wang, Flexible triboelectric generator, Nano Energy 1 (2012) 328–334.
[21] Z.L. Wang, On Maxwell's displacement current for energy and sensors: the origin of nanogenerators, Mater. Today 20 (2017) 74–82.
[22] Z.L. Wang, A.C. Wang, On the origin of contact-electrification, Mater. Today 30 (2019) 34–51.
[23] Y. Pang, Y. Fang, J. Su, et al., Soft ball-based triboelectric–electromagnetic hybrid nanogenerators for wave energy harvesting, Adv. Mater. Technol. 8 (2023) 2201246.
[24] Y. Zheng, T. Liu, J. Wu, et al., Energy conversion analysis of multilayered triboelectric nanogenerators for synergistic rain and solar energy harvesting, Adv. Mater. 34 (2022) 2202238.
[25] J. Gravesen, M. Willatzen, J. Shao, et al., Energy optimization of a mirror-symmetric spherical triboelectric nanogenerator, Adv. Funct. Mater. 32 (2022) 2110516.
[26] W. He, C. Shan, S. Fu, et al., Large harvested energy by self-excited liquid suspension triboelectric nanogenerator with optimized charge transportation behavior, Adv. Mater. 35 (2023) 2209657.
[27] Y. Li, S. Chen, H. Yan, et al., Biodegradable, transparent, and antibacterial alginate-based triboelectric nanogenerator for energy harvesting and tactile sensing, Chem. Eng. J. 468 (2023) 143572.
[28] Y. Li, X. Liu, Z. Ren, et al., Marine biomaterial-based triboelectric nanogenerators: insights and applications, Nano Energy 119 (2024) 109046.
[29] X. Shi, P. Chen, K. Han, et al., A strong, biodegradable, and recyclable all-lignocellulose fabricated triboelectric nanogenerator for self-powered disposable medical monitoring, J. Mater. Chem. A 11 (2023) 11730–11739.
[30] L. Wang, Y. Gao, J. Luo, et al., High-performance triboelectric nanogenerator based on NH_2-MXene/TiO_2@sodium alginate composite film for self-powered cathodic protection, Chem. Eng. J. 506 (2025) 159837.
[31] Y. Wen, F. Sun, Z. Xie, et al., Machine learning-assisted novel recyclable flexible triboelectric nanogenerators for intelligent motion, iScience 27 (2024) 109615.
[32] L. Zhang, B. Zhang, J. Chen, et al., Lawn structured triboelectric nanogenerators for scavenging sweeping wind energy on rooftops, Adv. Mater. 28 (2016) 1650–1656.
[33] W. Xu, H. Zheng, Y. Liu, et al., A droplet-based electricity generator with high instantaneous power density, Nature 578 (2020) 392–396.
[34] Y. Yang, X. Guo, M. Zhu, et al., Triboelectric nanogenerator enabled wearable sensors and electronics for sustainable internet of things integrated green earth, Adv. Energy Mater. 13 (2023) 2203040.
[35] J. Luo, K. Han, X. Wu, et al., Self-powered mobile sterilization and infection control system, Nano Energy 88 (2021) 106313.
[36] X. Li, J. Luo, K. Han, et al., Stimulation of ambient energy generated electric field on crop plant growth, Nat. Food 3 (2022) 133–142.
[37] L. Zhang, Y. Liao, Y.-C. Wang, et al., Cellulose II aerogel-based triboelectric nanogenerator, Adv. Funct. Mater. 30 (2020) 2001763.
[38] Y. Song, J. Bao, Y. Hu, et al., Ultra-porous cellulose nanofibril aerogel films as excellent triboelectric positive materials via direct freeze-drying of dispersion, Nano Energy 103 (2022) 107832.
[39] N. Meng, Y. Zhang, W. Liu, et al., Monolithic conjugated microporous polymer aerogel for triboelectric nanogenerator, Adv. Funct. Mater. 34 (2024) 2313534.
[40] X. Shi, X. Fan, Y. Zhu, et al., Pushing detectability and sensitivity for subtle force to new limits with shrinkable nanochannel structured aerogel, Nat. Commun. 13 (2022) 1119.
[41] J. Zhang, J. Zheng, M. Gao, et al., Nacre-mimetic nanocomposite aerogels with exceptional mechanical performance for thermal superinsulation at extreme conditions, Adv. Mater. 35 (2023) 2300813.
[42] F. Wang, S. Wang, Y. Liu, et al., Improved electrical output performance of cellulose-based triboelectric nanogenerators enabled by negative triboelectric materials, Small 20 (2024) 2308195.
[43] H. Oh, S.S. Kwak, B. Kim, et al., Highly conductive ferroelectric cellulose composite papers for efficient triboelectric nanogenerators, Adv. Funct. Mater. 29 (2019) 1904066.
[44] N. Wang, W. Zhang, Z. Li, et al., Dual-electric-polarity augmented cyanoethyl cellulose-based triboelectric nanogenerator with ultra-high triboelectric charge density and enhanced electrical output property at high humidity, Nano Energy 103 (2022) 107748.
[45] H. Shen, L. Wang, F. Zhang, et al., Fabrication of alginate-based bio-tribopositive films via amine modification and metal ion coordination for high surface charge density, Nano Energy 136 (2025) 110677.
[46] T. Li, C. Chen, A.H. Brozena, et al., Developing fibrillated cellulose as a sustainable technological material, Nature 590 (2021) 47–56.
[47] W. Song, X. Pan, X. Wang, et al., Load-bearing structure inspired cellulose-based aerogel with high resilience and water tolerance, Adv. Funct. Mater. 35 (2025) 2415937.
[48] Q. Zheng, L. Fang, H. Guo, et al., Highly porous polymer aerogel film-based triboelectric nanogenerators, Adv. Funct. Mater. 28 (2018) 1706365.
[49] J.-H. Pang, X. Liu, M. Wu, et al., Fabrication and characterization of regenerated cellulose films using different ionic liquids, J. Spectrosc. 2014 (2014) 214057.
[50] H. Qi, B. Schulz, T. Vad, et al., Novel carbon nanotube/cellulose composite fibers as multifunctional materials, ACS Appl. Mater. Interfaces 7 (2015) 22404–22412.
[51] E. Fukada, T. Furukawa, Piezoelectricity and ferroelectricity in polyvinylidene fluoride, Ultrasonics 19 (1981) 31–39.
[52] P. Martins, A.C. Lopes, S. Lanceros-Mendez, Electroactive phases of poly (vinylidene fluoride): determination, processing and applications, Prog. Polym. Sci. 39 (2014) 683–706.
[53] C. Park, K. Lee, M. Koo, et al., Soft ferroelectrics enabling high-performance intelligent photo electronics, Adv. Mater. 33 (2021) 2004999.
[54] Z. Zheng, X. Wang, G. Hang, et al., Recent progress on flexible poly(vinylidene fluoride)-based piezoelectric nanogenerators for energy harvesting and self-powered electronic applications, Renew. Sustain. Energy Rev. 193 (2024) 114285.
[55] Q. Li, G. Zhang, F. Liu, et al., Solution-processed ferroelectric terpolymer nanocomposites with high breakdown strength and energy density utilizing boron nitride nanosheets, Energy Environ. Sci. 8 (2015) 922–931.
[56] A. Salimi, A.A. Yousefi, Analysis method: FTIR studies of β-phase crystal formation in stretched PVDF films, Polym. Test. 22 (2003) 699–704.
[57] Y. Bormashenko, R. Pogreb, O. Stanevsky, et al., Vibrational spectrum of PVDF and its interpretation, Polym. Test. 23 (2004) 791–796.
[58] K. Lozano Montero, R. Calvo Guzman, A. Tewari, et al., Printed and stretchable triboelectric energy harvester based on P(VDF-TrFE) porous aerogel, Adv. Funct. Mater. 34 (2024) 2312881.
[59] V. Sencadas, M.V. Moreira, S. Lanceros-Méndez, et al., α- to β Transformation on PVDF Films Obtained by Uniaxial Stretch, Mater. Sci. Forum 514-516 (2006) 872–876.
[60] L. Li, X. Wang, Y. Hu, et al., Understanding the ferroelectric polymer–metal contact electrification for triboelectric nanogenerator from molecular and electronic structure, Adv. Funct. Mater. 32 (2022) 2109949.
[61] Y. Zhang, Z. Zhang, W. Peng, et al., Bionic wood-inspired structure enables aerogel film triboelectric material with humidity adaptation, Chem. Eng. J. 497 (2024) 154906.
[62] J. Hu, Y. Qian, F. Wei, et al., High powered output flexible aerogel triboelectric nanogenerator under ultrahigh temperature condition, Nano Energy 121 (2024) 109229.
[63] L. Li, R. Wang, Y. Fu, et al., Fabricating and engineering woody-biomass aerogels for high-performance triboelectric nanogenerators for energy harvesting and biomechanical monitoring, Adv. Funct. Mater. 35 (2025) 2412324.
[64] Q. Fu, Y. Liu, T. Liu, et al., Air-permeable cellulosic triboelectric materials for self-powered healthcare products, Nano Energy 102 (2022) 107739.

Muqi Chen is a Master degree candidate at College of Materials Science and Engineering, Ocean University of China. His research focuses on the smart sports applications based on triboelectric nanogenerators.

Minglan Ji received her bachelor degree in Physics from Shandong Normal University in 2023. Now she is a post-graduate student and major in Materials Science at the University of Chinese Academy of Sciences (UCAS). Her current research interest is self-powered systems based on triboelectric nanogenerators.

Lijun Huang received her bachelor degree in engineering from Harbin University of Science and Technology in 2021. She received her master degree in engineering from Guangxi University in 2024. She is currently a doctoral student and major in Materials Science in University of Chinese Academy of Sciences. Her research mainly focuses on triboelectric nanogenerators, self-powered systems, and wearable electronics.

Ning Wu received his B.S. degree in Computational Physics from Jiangxi Science and Technology Normal University, in 2018, and her Ph.D. degree in Condensed Matter Physics from Institute of Physics, Chinese Academy of Sciences in 2022. After graduation, he worked in Beijing Institute of Nanoenergy and Nanosystems as a postdoctoral research fellow. She is now an assistant professor in Beijing Institute of Nanoenergy and Nanosystems, Chinese Academy of Sciences. Her research interests include first-principles calculation, triboelectric nanogenerators, tribology, surface and interfacial properties of materials.

Tao Jiang received his BS and Ph.D. degrees in School of Materials Science and Engineering from East China University of Science and Technology, in 2008 and 2014, respectively. After graduation, he joined Beijing Institute of Nanoenergy and Nanosystems as a postdoctoral fellow. Now he is a professor at Beijing Institute of Nanoenergy and Nanosystems, Chinese Academy of Sciences. His research interests are the theoretical studies of triboelectric nanogenerators, and applications of TENGs in blue energy harvesting.

Chengyu Li is currently a doctoral student at University of Chinese Academy of Sciences. His research focuses on nanogenerators, embedded systems, wearable and flexible electronics for healthcare applications.

Wanpeng Li received his Ph.D. degree in Materials Science and Engineering from City University of Hong Kong in 2021. From 2021–2023, he worked as a postdoctoral researcher at the Time-resolved Aberration Corrected Environmental (TRACE) EM Unit at City University of Hong Kong, during which, he focused on TEM characterization of metallic materials and electron-beam sensitive materials. In 2023, he joined Beijing Institute of Nanoenergy and Nanosystems, Chinese Academy of Science, as an associate researcher. Now his research interests are ultrafast TEM and TEM characterization of low dimensional materials.

Boyang Yu received his B.S. degree in Applied Physics and Ph.D. degree in Electronic Science and Technology from Huazhong University of Science and Technology in 2017 and 2022, respectively. He is currently a postdoctoral research fellow at Beijing Institute of Nanoenergy and Nanosystems, Chinese Academy of Sciences. His research interest focuses on electrochemical heat harvesting, sensing and cooling.

Jianjun Luo received his B.S. degree in Applied Chemistry from Jinan University in 2013, and his Ph.D. degree in Condensed Matter Physics from University of Chinese Academy of Sciences in 2018. After graduation, he worked in Beijing Institute of Nanoenergy and Nanosystems as a postdoctoral research fellow. He is now an associate professor in Beijing Institute of Nanoenergy and Nanosystems, Chinese Academy of Sciences. His research interests include triboelectric nanogenerators, self-powered systems, and wearable electronics.

Xiaoyi Li received his BEng Degree from Southeast University in 2012. He received his Ph.D. of Materials Science and Engineering from Tsinghua University in 2017. He was also an exchange student of Beijing Institute of Nanoenergy and Nanosystems (BINN) during 2013–2018. After his graduate study, he worked as a Postdoctoral Fellow at the Chinese University of Hong Kong during 2018–2019. Dr Li joined the Ocean University of China as a full professor in December 2019, focusing on nano energy, self-powered systems and TENG applications in the ocean.

Zhong Lin Wang received his Ph.D. degree from Arizona State University in physics. He now is the chief scientist and director of the Beijing Institute of Nanoenergy and Nanosystems, Chinese Academy of Sciences. Prof. Wang has made original and innovative contributions to the synthesis, discovery, characterization and understanding of fundamental physical properties of oxide nanobelts and nanowires, as well as applications of nanowires in energy sciences, electronics, optoelectronics and biological science. His discovery and breakthroughs in developing nanogenerators establish the principle and technological road map for harvesting mechanical energy from environmental and biological systems for powering personal electronics. His research on self-powered nanosystems has inspired the worldwide efforts in academia and industry for studying energy for micro-nano-systems, which is now a distinct disciplinary in energy research and future sensor networks. He coined and pioneered the fields of piezotronics and piezophototronics by introducing piezoelectric potential gated charge transport process in fabricating new electronic and optoelectronic devices.